Research Article Vol. 30, No. 17 / 15 Aug 2022 / Optics Express 31472
Optics EXPRESS

Likelihood based synchronization algorithms in optical pulse position modulation systems with photon-counting receivers

YA-TIAN LI,[1,*] TIAN-WEN GENG,[1] AND SHI-JIE GAO[1,2]

[1] Changchun Institute of Optics, Fine Mechanics and Physics, Chinese Academy of Sciences, Changchun 130033, China
[2] University of Chinese Academy of Sciences, Beijing 100049, China
[*] yt_li@ciomp.ac.cn

Abstract: Deep space optical communication (DSOC) is becoming a hot topic. Pulse position modulation (PPM) is an effective tool to realize DSOC benefiting from the feature of high sensitivity. In this paper, we analyze 2×1 optical PPM systems with photon-counting detectors, where the distance difference between the two links causes asynchronous superpositions at the receiving end. Two synchronization algorithms are proposed to estimate the time offsets of the two links, which are the optimal Global Maximum Likelihood Estimation (GMLE) and the suboptimal Integer Comparison - Fractional Likelihood Estimation (ICFLE). The complexities of the two methods are also compared. In order to measure the two proposed algorithms, the Cramer-Rao bounds (CRB) are derived. According to simulation results, both the two proposed algorithms approach the deduced CRBs. Furthermore, an equivalent experiment is designed to verify the feasibility and effectiveness of the proposed algorithms. It's also indicated that the proposed algorithms may be utilized in practical systems.

1. Introduction

Deep space optical communication (DSOC) can provide high transmission rates than traditional radio frequency (RF) techniques [1,2]. By utilizing narrow pulses, the pulse position modulation (PPM) has the ability of reaching the required data rates. Benefiting from the feature of high sensitivity, the PPM scheme has become an effective tool to realize DSOC [3]. One of the typical applications is the NASA's Lunar Laser Communication Demonstration (LLCD) mission, which has made a great success that the lunar orbiter was able to realize the 622Mb/s laser communication between the moon and the ground by only 0.5 watts of laser power [4]. In order to detect a PPM symbol, the receiver determines whether there is a pulse in the current slot, where the photon-counting detectors are widely employed [5,6].

1.1. Related works

To the best of the authors' knowledge, the existing works on the optical PPM systems can be divided into two categories, which are perfect synchronous receivers and imperfect asynchronous receivers, respectively. In the first category, it's assumed the perfect synchronization happens, where most literature focuses primarily on performance analysis. In Ref. [7], bit error rate (BER) expressions of the M-ary PPM scheme variations against the changes in different parameters are investigated , where a Gaussian laser beam propagates in non-Kolmogorov turbulence. Ref. [8] has conducted an exhaustive symbol error rate (SER) analysis of the optical spatial PPM MIMO (multi-input multi-output) system over arbitrarily correlated Gamma-Gamma turbulent fading channels. In Ref. [9], the performance analysis of L-ary PPM with an avalanche photodiode (APD) receiver is investigated for a ground-station-to-low-Earth-orbit laser link, where spatial diversity is implemented in the transmitter side, i.e., the multiple-in single-out (MISO) scenario.

#467571 https://doi.org/10.1364/OE.467571
Journal © 2022 Received 10 Jun 2022; revised 28 Jul 2022; accepted 1 Aug 2022; published 12 Aug 2022

In the second category, the imperfect synchronization schemes are analyzed, where several imperfect compensation methods are presented. Ref. [10] proposes a modified channel likelihood algorithm for optical communication systems where photon-counting events are impaired by undesirable dead time and jitters. Ref. [11] evaluates the BER performance of optical waves propagating in the non-Kolmogorov coronal turbulence, where coronal turbulence is considered during superior solar conjunction. Ref. [12] analyzes the asynchronous sampling effect between the reference clock in the PPM transmitter and the slave clock in the receiver, where a new error probability expression is derived for the occurrence of slot-period misalignment. A dynamic slot period realignment technique is further proposed to mitigate the slot-period misalignment problem. In Ref. [13], the phase modulation jitter is estimated with the help of a maximum a posteriori probability (MAP) estimator, which approaches the minimum probability of error performance. In Ref. [14], a maximum likelihood estimator is established to obtain the slot offset between the transmitter and the receiver.

Diversity technique is designed to provide diverse replicas of transmitted symbols [15–17]. Different from RF systems, it has been proved that the repetition codes (RC) outperform orthogonal space-time block codes (OSTBC) in intensity modulation/direct detection (IM/DD) optical links [18]. As a result, diversity technique with RC scheme can be further utilized to improve the reliability in PPM DSOC systems.

1.2. Motivation and contribution

Although there are several papers considering the optical PPM systems in diversity mode [8,9,19–21], most of these papers make the assumption of perfect synchronization. In addition, the papers focusing on imperfect synchronization mainly consider the point-to-point scene. To the authors' best knowledge, there is no existing paper discussing the imperfect synchronization issue in optical PPM MISO systems with photon-counting detectors. As a result, this paper studies a 2×1 MISO optical PPM system with a photon-counting receiver, where the distance difference between the two links causes asynchronous superpositions of signals at the receiving end. Motivated by the estimation methods in Ref. [13,14], this paper is committed to estimate the values of the timing offsets, where each offset is determined by the receiver and corresponding transmitter. The main contributions are summarized below.

■ Different from abovementioned literatures on the synchronization issue of point-to-point scenes, this paper considers the synchronization problem in 2×1 MISO optical PPM systems with photon-counting receivers.

■ Two algorithms are proposed to estimate the offsets, which are the optimal Global Maximum Likelihood Estimation (GMLE) algorithm and the suboptimal Integer Comparison - Fractional Likelihood Estimation (ICFLE) algorithm. We also compare the complexities of the two algorithms.

■ The Cramer Rao bounds (CRB) are further deduced to evaluate effectiveness of the proposed algorithms. It's verified by simulations that the two algorithms both approach the derived CRB.

■ An equivalent experiment is set up, which indicates that the proposed algorithms have the potential to be employed in practical systems.

1.3. Paper structure

The remainder of this paper is organized as follows. The system structure is described in Sec. 2. The proposed optimal GMLE and suboptimal ICFLE algorithms are illustrated in Sec. 3.1 and Sec. 3.2, respectively. In addition, the estimation bias and complexity analysis are given in Sec. 3.3. In order to measure the two proposed algorithms, the CRBs are derived in Sec. 4. We provide simulation results and the equivalent experimental results in Sec. 5.1 and Sec. 5.2, respectively. In the end, the conclusions are drawn. It's also mentioned that the variables are illustrated as the lowercase italic forms. Besides, all the vectors have the lowercase bold forms. For ease of reading, definitions of the main variables are summarized in Table 1.

Table 1. Definition of main variables

Symbol	Definition
τ_1, τ_2	Timing offset between TX-1 (or TX-2) and the receiver RX
i_1, i_2	Integer part of τ_1, τ_2
$\varepsilon_1, \varepsilon_2$	Fractional part of τ_1, τ_2
K_b	Average number of background photon counts
K_s	Average number of signal photon counts per symbol
N	Number of integration symbols
M, P	Number of data slots (or guard slots) per symbol
$\lambda_n(\tau_1, \tau_2)$	Intensity function for the n-th slot
$x_p[n]$	Number of photons in the n-th slot of the p-th received symbol
y_n	Cyclic addition of $x_p[n]$ with $p = 0, 1, 2, \ldots, N-1$
$\hat{\bullet}$	Estimated value of $\bullet$
$C_{\varepsilon_1}, C_{\varepsilon_2}$	Cramer-Rao bounds for $\varepsilon_1, \varepsilon_2$

2. System model

The system model is illustrated in Fig. 1. In the 2×1 MISO system described in Fig. 1, two optical links are established with the data modulated by PPM, i.e., TX-1 to RX and TX-2 to RX. According to Fig. 1, τ_1 (or τ_2) is supposed to be the timing offset between TX-1 (or TX-2) and the receiver RX, which has been normalized by a slot interval. As a positive real number, τ_1 and τ_2 can be divided into integer part and fractional part, as shown in Eq. (1).

$$\tau_1 = i_1 + \varepsilon_1, \;\; i_1 = \lfloor \tau_1 \rfloor ; \quad \tau_2 = i_2 + \varepsilon_2, \; i_2 = \lfloor \tau_2 \rfloor , \tag{1}$$

where $\lfloor \bullet \rfloor$ denotes the round down operator. In an arbitrary PPM symbol, there are M data slots and P guard slots, where $\log_2 M$ data bits are carried. This paper assumes the guard slots are longer than the offsets difference, i.e., $|\tau_2 - \tau_1| < P$. In other words, the guard slots guarantee to eliminate the inter-symbol interference (ISI). However, the data slots still asynchronously superimpose in one PPM symbol. Due to the existence of τ_1 and τ_2, the receiving end becomes no longer ideal. The number of signal photons in each time slot is determined by the number of signal photons from TX-1 and TX-2. Owing to the reciprocity of τ_1 and τ_2, this paper assumes that the distance of the TX-2-to-RX link is longer than the TX-1-to-RX link. Let's take the TX-1-to-RX link as an example. The mean number of photon counts is equal to $(1 - \varepsilon_1) \cdot K_s + K_b$ in the i_1-th slot, while the average number of photon counts is equal to $\varepsilon_1 \cdot K_s + K_b$ in the $i_1 + 1$-th slot. K_b and K_s are supposed to be the mean number of background photon counts and the average number of signal photon counts per symbol, respectively.

Since the photons from TX-1 and TX-2 are superimposed on each other, the number of photons after superposition still keeps the Poisson distribution. We define $x_p[n]$ ($n = 0, 1, 2, \ldots, M+P-1$) to be the number of photons in the n-th slot of the p-th received symbol. In order to estimate τ_1 and τ_2, the observed slots are binned into a vector $\mathbf{y} = [y_0, y_1, \ldots, y_{M+P-1}]$ by cyclic additions with the period of $M + P$, The n-th element in $\mathbf{y}$ is $y_n = \sum_{p=0}^{N-1} x_p[n]$, where N is defined as the number of integration symbols. Obviously, y_n also obeys Poisson distribution, whose probability

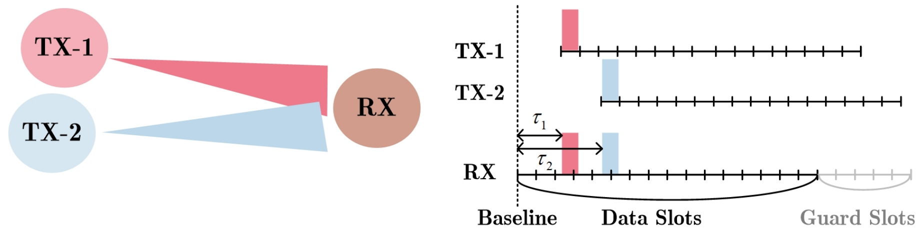

Fig. 1. The system structure of an M-to-1 OWC system.

mass function (PMF) is given in Eq. (2),

$$P_{y_n|\boldsymbol{\tau}}\left(y_n \mid \boldsymbol{\tau}\right) = \frac{1}{y_n!}\lambda_n(\tau_1,\tau_2)^{y_n}\exp\left(-\lambda_n(\tau_1,\tau_2)\right), \tag{2}$$

where the vector $\boldsymbol{\tau}$ is short for $[\tau_1, \tau_2]$. $\lambda_n(\tau_1, \tau_2)$ is the intensity function for the n-th slot,which is shown in Eq. (3).

$$\lambda_n(\tau_1,\tau_2) = \begin{cases} (1-\varepsilon_1)\,\frac{N}{M}K_s + NK_b,\;\; n = i_1 \mod (M+P) \\ \frac{N}{M}K_s + NK_b,\;\; n = i_1+1,\ldots,i_2+1, i_1+M+1,\ldots,i_2+M-1 \mod (M+P) \\ (2-\varepsilon_2)\,\frac{N}{M}K_s + NK_b,\;\; n = i_2 \mod (M+P) \\ \frac{2N}{M}K_s + NK_b,\;\; n = i_2+1,\ldots,i_1+M-1 \mod (M+P) \\ (1+\varepsilon_1)\,\frac{N}{M}K_s + NK_b,\;\; n = i_1+M \mod (M+P) \\ (\varepsilon_2)\,\frac{N}{M}K_s + NK_b,\;\; n = i_2+M \mod (M+P) \\ NK_b,\;\; n = i_2+M+1,..,M+P-1,0,\ldots,i_1-1 \mod (M+P) \end{cases} \tag{3}$$

For an intuitive description the intensity function, Fig. 2 gives two examples of $\lambda_n(\tau_1, \tau_2)$, with $\boldsymbol{\tau} = [2.5,\ 6.2]$ in Fig. 2(a) and $\boldsymbol{\tau} = [14.5,\ 18.2]$ in Fig. 2(b). So far, we can summarize the problem to be solved is to estimate the values of τ_1 and τ_2 according to the observation space of photons $\{x_p[n]\}_p$ in these slots. In order to minimize the influence of noise, we cyclically add the observed $\{x_p[n]\}_p$ to transform into an equivalent observation vectors $\mathbf{y}$. Two proposed algorithms will be further depicted in Sec. 3. It should be mentioned that our proposed algorithms can be applied in the receiver of a 2 × 1 MISO optical PPM system just after a photon-counting

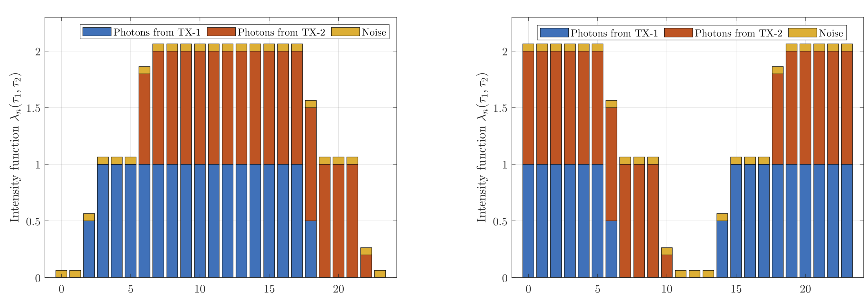

(a) $\tau_1 = 2.5,\ \ \tau_2 = 6.2$

(b) $\tau_1 = 14.5,\ \ \tau_2 = 18.2$

Fig. 2. Two examples of $\lambda_n(\tau_1, \tau_2)$.

Optics EXPRESS

detector. The detector detects the measured photons' number in each slots, which provides the input of the corresponding module of the GMLE algorithm (or the ICFLE algorithm). In the sequel, our algorithm sends the estimated offsets to the subsequent equalization module to eliminate the interference.

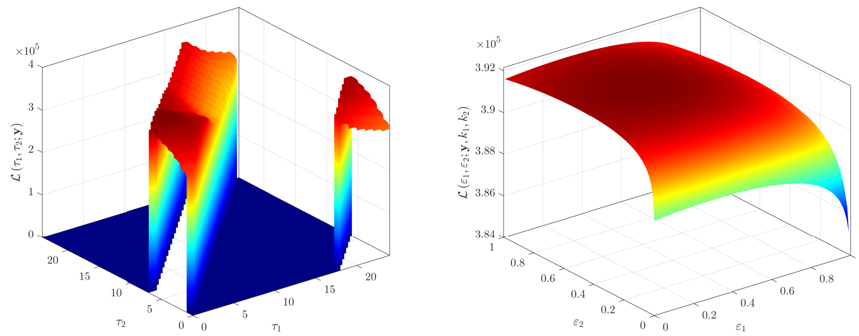

(a) (b)

Fig. 3. An example of likelihood functions, (a)$\mathcal{L}\left(\tau_1, \tau_2; \mathbf{y}\right)$ (b) $\mathcal{L}\left(\varepsilon_1, \varepsilon_2; \mathbf{y}, k_1, k_2\right)$.

3. Estimation algorithms

3.1. Optimal GMLE algorithm

On the basis of Eqs. (2) and (3), the log likelihood function $\mathcal{L}\left(\tau_1, \tau_2; \mathbf{y}\right)$ can be obtained by Eq. (4). The likelihood function in this section characterizes the magnitude of the joint distribution function for the timing offsets τ_1 and τ_2, when the number of photons within each slot is obtained.

$$\begin{aligned}\mathcal{L}\left(\tau_1, \tau_2; \mathbf{y}\right) &= \sum\nolimits_{n=0}^{M+P-1} \log P_{\mathbf{y}_n|\boldsymbol{\tau}}\left(y_n \left|\tau_1, \tau_2\right.\right) \\ &= \sum\nolimits_{n=0}^{M+P-1} y_n \cdot \log\left[\lambda_n\left(\tau_1, \tau_2\right)\right] - \lambda_n\left(\tau_1, \tau_2\right) - \log\left[y_n!\right]\end{aligned} \tag{4}$$

Since the sums of the second terms (or the third terms) are constant, which can be ignored. Under normal thinking, our next step is to find the partial derivatives of τ_1 and τ_2 to solve their values. However, $\mathcal{L}\left(\tau_1, \tau_2; \mathbf{y}\right)$ is not differentiable if either τ_1 or τ_2 is an integer, which is shown in Fig. 3(a). What's more, $\lambda_n\left(\tau_1 - i, \tau_2 - j\right), (i, j = 0, 1, \ldots, M + P - 1)$ is not equal to the cyclic shift of $\lambda_n\left(\tau_1, \tau_2\right)$, which is different from the circumstance $\lambda_n(\tau) = \lambda_0((\tau - n) \mod (M + P))$ in a point-to-point communication scenario in Ref. [14]. Fortunately, when τ_1 and τ_2 are in the integer intervals ($\tau_1 \in (i, i+1)$, $\tau_2 \in (j, j+1)$, $i, j = 0, 1, \ldots, M + P - 2$), the likelihood function $\mathcal{L}\left(\tau_1, \tau_2; \mathbf{y}\right)$ is both differentiable for the variables τ_1, τ_2. For the convenience of representation, this paper defines the range $\langle i, j\rangle$ as the abbreviation of the integer interval $\tau_1 \in (i, i+1)$, $\tau_2 \in (j, j+1)$. As a sum of concave functions of affine functions, the likelihood function keeps concave in each integer interval [22]. Our proposed GMLE algorithm comes into being, where we first estimate potential values for τ_1 and τ_2 in each integer interval of interest, and choose the final correct value in these sets of potential values.

To describe the likelihood function within each interval, $\mathcal{L}\left(\varepsilon_1, \varepsilon_2; \mathbf{y}, k_1, k_2\right)$ is defined to be the log likelihood function in the integer interval $\tau_1 \in (k_1, k_1 + 1)$, $\tau_2 \in (k_2, k_2 + 1)$, i.e.,

$\mathcal{L}(\varepsilon_1, \varepsilon_2; \mathbf{y}, k_1, k_2) = \mathcal{L}(\tau_1, \tau_2; \mathbf{y})\big|_{\tau_1 \in (k_1, k_1+1), \tau_2 \in (k_2, k_2+1)}$, which is simplified by Eq. (5).

$$\begin{aligned}\mathcal{L}(\varepsilon_1, \varepsilon_2; \mathbf{y}, k_1, k_2) = C + y_{k_1} \cdot \log\left[(1-\varepsilon_1)\tfrac{N}{M}K_s + N \cdot K_b\right] + y_{k_2} \cdot \log\left[(2-\varepsilon_2)\tfrac{N}{M}K_s + N \cdot K_b\right] \\ + y_{k_1+M} \cdot \log\left[(1+\varepsilon_1)\tfrac{N}{M}K_s + N \cdot K_b\right] + y_{k_2+M} \cdot \log\left[\varepsilon_2 \tfrac{N}{M}K_s + N \cdot K_b\right]\end{aligned}, \tag{5}$$

where C represents the parts unrelated to ε_1 and ε_2. An example of $\mathcal{L}(\varepsilon_1, \varepsilon_2; \mathbf{y}, k_1, k_2)$ is illustrated in Fig. 3(b) with $k_1 = i_1$, $k_2 = i_2$. Intuitively, the function $\mathcal{L}(\varepsilon_1, \varepsilon_2; \mathbf{y}, k_1, k_2)$ is differentiated and concave.

The next thing we need to do is to find the estimates of ε_1 and ε_2 in the selected range $\langle k_1, k_2 \rangle$. The partial derivatives of ε_1 and ε_2 are derived in Eqs. (6) and (7), respectively.

$$\frac{\partial \mathcal{L}}{\partial \varepsilon_1} = -y_{k_1}\frac{\frac{N}{M}K_s}{(1-\varepsilon_1)\frac{N}{M}K_s + N \cdot K_b} + y_{k_1+M}\frac{\frac{N}{M}K_s}{(1+\varepsilon_1)\frac{N}{M}K_s + N \cdot K_b} \tag{6}$$

$$\frac{\partial \mathcal{L}}{\partial \varepsilon_2} = -\frac{y_{k_2}\frac{N}{M}K_s}{(2-\varepsilon_2)\frac{N}{M}K_s + N \cdot K_b} + \frac{y_{k_2+M}\frac{N}{M}K_s}{\varepsilon_2\frac{N}{M}K_s + N \cdot K_b} \tag{7}$$

By setting the partial derivatives to 0, the estimated values in the interval $\langle k_1, k_2 \rangle$ is obtained, shown in Eqs. (8) and (9), respectively.

$$\hat{\varepsilon}_{1,\langle k_1,k_2\rangle} = \frac{\left(y_{(k_1+M) \bmod (M+P)} - y_{k_1}\right)\left(\frac{N}{M}K_s + N \cdot K_b\right)}{\frac{N}{M}K_s\left(y_{k_1} + y_{(k_1+M) \bmod (M+P)}\right)} \tag{8}$$

$$\hat{\varepsilon}_{2,\langle k_1,k_2\rangle} = \frac{2y_{(k_2+M) \bmod (M+P)}\frac{N}{M}K_s + \left(y_{(k_2+M) \bmod (M+P)} - y_{k_2}\right)N \cdot K_b}{\frac{N}{M}K_s\left(y_{k_2} + y_{(k_2+M) \bmod (M+P)}\right)} \tag{9}$$

Therefore, the final estimation values $\hat{\tau}_1$ and $\hat{\tau}_2$ can be obtained by

$$\begin{aligned}&\hat{\tau}_1 = \hat{i}_1 + \hat{\varepsilon}_{1,\langle \hat{i}_1,\hat{i}_2\rangle}, \qquad \hat{\tau}_2 = \hat{i}_2 + \hat{\varepsilon}_{2,\langle \hat{i}_1,\hat{i}_2\rangle} \\ &s.t.\ \left(\hat{i}_1, \hat{i}_2\right) = \arg\max_{(k_1,k_2)} \mathcal{L}(\varepsilon_1, \varepsilon_2; \mathbf{y}, k_1, k_2)\big|_{\varepsilon_1=\hat{\varepsilon}_{1,\langle k_1,k_2\rangle}, \varepsilon_2=\hat{\varepsilon}_{2,\langle k_1,k_2\rangle}}\end{aligned}. \tag{10}$$

The pseudo-code diagram for the proposed GMLE algorithm is given in Tab.2.

Table 2. The pseudo code diagram of the proposed optimal GMLE algorithm. cmc

GMLE Algorithm	
1:	Calculate the vector $\mathbf{y}$ by cyclicly adding $x_p[n]\,(n = 0, 1, 2, \ldots, M+P-1)$.
2:	**for** $k_1 = 0, 1, 2, \ldots, M+P-1$ **do**
3:	**for** $k_2 = k_1+1, k_1+1, 2, \ldots, k_1+P$ **do**
4:	Obtain fractional part $\hat{\varepsilon}_{1,\langle k_1,k_2\rangle}$ by Eq. (8).
5:	Obtain fractional part $\hat{\varepsilon}_{2,\langle k_1,k_2\rangle}$ by Eq. (9).
6:	Calculate $\mathcal{L}\left(\hat{\varepsilon}_{1,\langle k_1,k_2\rangle}, \hat{\varepsilon}_{2,\langle k_1,k_2\rangle}; \mathbf{y}, k_1, k_2\right)$ in interval $\langle i, j\rangle$ by Eq. (5).
7:	**end for**
8:	**end for**
9:	Derive final estimated values $\hat{\tau}_1$ and $\hat{\tau}_2$ by Eq. (10).

3.2. Suboptimal ICFLE algorithm

The GMLE algorithm described above needs to estimate each possible $\langle k_1, k_2 \rangle$ interval, find the possible values for $\hat{\tau}_1$ and $\hat{\tau}_2$, and then determine the final estimation by choosing among the sets of possible values that maximizes the likelihood function. In order to reduce the amount of computation, we propose a suboptimal ICFLE algorithm. Let's recap Eq. (2), there will be $P-(i_2-i_1)-1$ continuous noise slots, due to $\lambda_n(\tau_1,\tau_2) = NK_b, n = i_2+M+1,\ldots, M+P-1, 0, \ldots, i_1-1 \mod (M+P)$. This circumstance can be clearly seen in Fig. 2. Although the value of i_1 is changing, as long as the value of i_2-i_1 remains unchanged ($i_2-i_1=4$ in Fig. 2), the number of noise time slots is a fixed value (3 slots). In other words, if we find the consecutive time slots with a few photons, i_1 and i_2 can be estimated. These consecutive time slots' numbers are defined by a vector $\mathbf{f}$. Then the estimation on i_1 and i_2 can be obtained by Eq. (11).

$$\hat{i}_{1,\text{sub}} = \mod(\mathbf{f}(\text{end})+1, M+P); \hat{i}_{2,\text{sub}} = \mod(\mathbf{f}(1)-M-1, M+P) \tag{11}$$

After estimating the integer parts, the fractional parts can be derived in the way similar as GMLE, given in Eqs. (12) and (13).

$$\hat{\varepsilon}_{1,\text{sub}} = \frac{\left(y_{(\hat{i}_{1,\text{sub}}+M) \bmod (M+P)} - y_{\hat{i}_{1,\text{sub}}}\right)\left(\frac{N}{M}K_s + N\cdot K_b\right)}{\frac{N}{M}K_s\left(y_{\hat{i}_{1,\text{sub}}} + y_{(\hat{i}_{1,\text{sub}}+M) \bmod (M+P)}\right)} \tag{12}$$

$$\hat{\varepsilon}_{2,\text{sub}} = \frac{2y_{\hat{i}_{2,\text{sub}}+M}\frac{N}{M}K_s + \left(y_{\hat{i}_{2,\text{sub}}+M} - y_{\hat{i}_{2,\text{sub}}}\right)N\cdot K_b}{\frac{N}{M}K_s\left(y_{\hat{i}_{2,\text{sub}}} + y_{\hat{i}_{2,\text{sub}}+M}\right)} \tag{13}$$

At this point, we can obtain the estimates $\hat{\tau}_{1,\text{sub}} = \hat{i}_{1,\text{sub}} + \hat{\varepsilon}_{1,\text{sub}}$ and $\hat{\tau}_{2,\text{sub}} = \hat{i}_{2,\text{sub}} + \hat{\varepsilon}_{2,\text{sub}}$ by the suboptimal ICFLE algorithm. The pseudo-code diagram for the proposed ICFLE algorithm is given in Tab.3.

Table 3. The pseudo code diagram of the proposed suboptimal ICFLE algorithm. cmc

ICFLE Algorithm	
1:	Calculate the vector $\mathbf{y}$ by cyclicly adding $x_p[n]$ ($n = 0, 1, 2, \ldots, M+P-1$).
2:	Find the consecutive time slots $\mathbf{f}$ with a few photons in $\mathbf{y}$.
3:	Obtain the estimated integer parts i_1 and i_2 by Eq. (11).
4:	Obtain fractional part $\hat{\varepsilon}_{1,\text{sub}}$ by Eq. (12).
5:	Obtain fractional part $\hat{\varepsilon}_{2,\text{sub}}$ by Eq. (13).
6:	Derive final estimated values $\hat{\tau}_{1,\text{sub}} = \hat{i}_{1,\text{sub}} + \hat{\varepsilon}_{1,\text{sub}}$, $\hat{\tau}_{2,\text{sub}} = \hat{i}_{2,\text{sub}} + \hat{\varepsilon}_{2,\text{sub}}$.

3.3. Estimation bias and complexity analysis

In this subsection, we first prove that the proposed estimation algorithms are unbiased, and then compare their complexities. To facilitate discussion, we study the unbiased estimation of the fractional parts. The estimated unbiasedness will be verified in the numerical results. The

Optics EXPRESS

mathematical expectation of the estimated values are

$$\mathbb{E}\left[\hat{\varepsilon}_1\right] = \frac{\left(\mathbb{E}\left[y_{(i_1+M) \bmod (M+P)}\right] - \mathbb{E}\left[y_{i_1}\right]\right)\left(\frac{N}{M}K_s + N\cdot K_b\right)}{\frac{N}{M}K_s\left(\mathbb{E}\left[y_{i_1}\right] + \mathbb{E}\left[y_{(i_1+M) \bmod (M+P)}\right]\right)} = \frac{2\varepsilon_1 \frac{N}{M}K_s\left(\frac{N}{M}K_s + N\cdot K_b\right)}{2\frac{N}{M}K_s\left(\frac{N}{M}K_s + N\cdot K_b\right)} = \varepsilon_1, \tag{14}$$

$$\begin{aligned}\mathbb{E}\left[\hat{\varepsilon}_2\right] &= \frac{2\mathbb{E}\left[y_{(i_2+M) \bmod (M+P)}\right]\frac{N}{M}K_s + \left(\mathbb{E}\left[y_{(i_2+M) \bmod (M+P)}\right] - \mathbb{E}\left[y_{i_2}\right]\right)N\cdot K_b}{\frac{N}{M}K_s\left(\mathbb{E}\left[y_{i_2}\right] + \mathbb{E}\left[y_{(i_2+M) \bmod (M+P)}\right]\right)} \\ &= \frac{2\varepsilon_2\frac{N}{M}K_s\left(\frac{N}{M}K_s + N\cdot K_b\right)}{2\frac{N}{M}K_s\left(\frac{N}{M}K_s + N\cdot K_b\right)} = \varepsilon_2.\end{aligned} \tag{15}$$

Since all the elements of the vector $\mathbf{y}$ satisfy the Poisson distribution, the following mathematical expectations can be obtained, which are $\mathbb{E}\left[y_{(i_1+M) \bmod (M+P)}\right] = (1+\varepsilon_1)\frac{N}{M}K_s + N\cdot K_b$, $\mathbb{E}\left[y_{k_2}\right] = (2-\varepsilon_2)\frac{N}{M}K_s + N\cdot K_b$, $\mathbb{E}\left[y_{k_2}\right] = (2-\varepsilon_2)\frac{N}{M}K_s + N\cdot K_b$, $\mathbb{E}\left[y_{y_{(i_2+M) \bmod (M+P)}}\right] = \varepsilon_2\frac{N}{M}K_s + N\cdot K_b$. By substituting these mathematical expectations into Eqs. (14) and (15), we can get $\mathbb{E}\left[\hat{\varepsilon}_1\right] = \varepsilon_1$, $\mathbb{E}\left[\hat{\varepsilon}_2\right] = \varepsilon_2$. That is to say, the proposed estimations are unbiased.

In complexity analysis, we only consider operations between variables, and do not consider operations between variables and constants and between constants and constants, because the complexities of the latter two cases is much less than the operations between variables. The complexity comparison is given in Tab.4. As can be seen from Tab.4, the suboptimal ICFLE requires fewer operations than GMLE, which is caused by two reasons. First, the ICFLE algorithm only needs to estimate the fractional part once, while GMLE has to estimate the fractional part $P^2 + MP - M - P$ times. More importantly, in the ICTLE algorithm, there is no need to calculate the likelihood function value, so the logarithmic operations are omitted.

Table 4. Complexity analysis of two proposed algorithm.

Operation	GMLE	ICFLE
Multiplication	$4P^2 + 4MP - 4M - 4P$	-
Division	$2P^2 + 2MP - 2M - 2P$	2
Addition	$12P^2 + 12MP + N - 12M - 12P - 1$	$\frac{(P-1)P}{2} + N + 6$
Logarithm	$4P^2 + 4MP - 4M - 4P$	-
Comparators	$P^2 + MP - M - P$	$\frac{M^2+P^2-M-P}{2}$

4. Cramer Rao Bounds

In order to evaluate the performance of the proposed estimation algorithms, CRB should be illustrated, which is the lower bound of the mean square errors (MSE) of the estimated values. The CRB is the inverse of Fisher information matrix [23]. The Fisher information matrix is given in Eq. (16).

$$\mathbf{J} = \begin{bmatrix} \mathbb{E}\left[-\frac{\partial^2 \mathcal{L}(\varepsilon_1,\varepsilon_2;\mathbf{y},k_1,k_2)}{\partial\varepsilon_1^2}\right] & 0 \\ 0 & \mathbb{E}\left[-\frac{\partial^2 \mathcal{L}(\varepsilon_1,\varepsilon_2;\mathbf{y},k_1,k_2)}{\partial\varepsilon_2^2}\right] \end{bmatrix} \tag{16}$$

Then the CRB matrix $\mathbf{C}_\varepsilon$ is derived in Eq. (17),

$$\mathbf{C}_\varepsilon = \mathbf{J}^{-1} = \begin{bmatrix} C_{\varepsilon_1} & 0 \\ 0 & C_{\varepsilon_2} \end{bmatrix}, \tag{17}$$

Optics EXPRESS

where C_{ε_1} and C_{ε_2} represent the CRB for ε_1 and ε_2, given in Eqs. (18) and (19), respectively.

$$C_{\varepsilon_1} = \frac{\left(1-\varepsilon_1^2\right) K_s^2 + 2MK_sK_b + M^2K_b^2}{2K_s^2\left(\frac{N}{M}K_s + N\cdot K_b\right)} \tag{18}$$

$$C_{\varepsilon_2} = \frac{\left(2\varepsilon_2-\varepsilon_2^2\right) K_s^2 + 2MK_sK_b + M^2K_b^2}{2K_s^2\left(\frac{N}{M}K_s + N\cdot K_b\right)} \tag{19}$$

As can be seen from Eqs. (18) and (19), the CRB C_{ε_1} (or C_{ε_2}) can be determined by fractional part of the offset ε_1 (or ε_2), average number of background photon counts K_b, average number of signal photon counts per symbol K_s, the PPM order M and the number of integration symbols N. To compare C_{ε_1} and C_{ε_2}, we take the difference of C_{ε_1} and C_{ε_2} in Eq. (20).

$$C_{\varepsilon_1} - C_{\varepsilon_2} = \frac{\left[\left(1-\varepsilon_2\right)^2 - \varepsilon_1^2\right] K_s^2}{2K_s^2\left(\frac{N}{M}K_s + N\cdot K_b\right)} \propto \left[\left(1-\varepsilon_2\right)^2 - \varepsilon_1^2\right] \tag{20}$$

In this sequel, the relationship between C_{ε_1} and C_{ε_2} is deduced.

$$\begin{cases} C_{\varepsilon_1} < C_{\varepsilon_2}, & \text{if } \ \varepsilon_1 + \varepsilon_2 > 1 \\ C_{\varepsilon_1} > C_{\varepsilon_2}, & \text{if } \ \varepsilon_1 + \varepsilon_2 < 1 \end{cases} \tag{21}$$

5. Numerical performance

5.1. Simulation results

In this subsection, simulation results are illustrated. During the simulation, the default values of K_s and K_b are 0.25 and 5×10^{-5}, respectively. Every PPM symbol has $M = 16$ data slots and $P = 8$ guard slots. The number of integration symbols N is set to 10^5 by default. Figs. 4 and 5 show the MSE performance versus integration symbols N and the MSE performance versus average number of signal photon counts per symbol K_s. Among them, Figs. 4(a) and 5(a) show the results of estimating τ_1, while Figs. 4(b) and 5(b) depict the results of estimating τ_2. According to Figs. 4 and 5, both the proposed GMLE and ICFLE algorithms gradually approach the CRB with the increasing of integration symbols N (or average signal photon counts per symbol K_s), which shows the effectiveness of the proposed algorithm. It's also found that the suboptimal ICFLE is worse than the optimal GMLE in the case of either fewer signal photons or fewer integration symbols. However, the gap between the optimal GMLE and suboptimal ICFLE gets smaller with the horizontal axis increases. The reason is that the situation of fewer signal photons (or fewer integration symbols) represents a low signal-to-noise ratio scene (SNR). The estimated values of the integer parts $\hat{i}_{1,\mathrm{sub}}, \hat{i}_{2,\mathrm{sub}}$ by ICFLE have a large probability to deviate from the true value i_1, i_2, resulting in a large MSE value. However, with the increase of SNR, the estimated integer parts are gradually accurate, which makes that the ICFLE algorithm gradually close to the GMLE algorithm.

The CRBs for τ_1 and τ_2 are illustrated in Fig. 6, where cases of $\varepsilon_1 = \varepsilon_2$, $\varepsilon_1 = 2\varepsilon_2$, $2\varepsilon_1 = \varepsilon_2$ are analyzed in Fig. 6(a), 6(b) and 6(c), respectively. According to Fig. 6, their CRBs change in opposite directions as ε_1 and ε_2 increase. Among them, C_{ε_1} is inversely correlated with ε_1, and C_{ε_2} is positively correlated with ε_2. The reasons for this phenomenon are as follows. Looking back at Eqs. (18) and (19), we can ignore K_b under large SNR conditions, resulting in $C_{\varepsilon_1} \propto \left(1-\varepsilon_1^2\right)$, $C_{\varepsilon_2} \propto \left(2\varepsilon_2-\varepsilon_2^2\right)$. Besides the monotonicity of CRBs, we can obtain from Fig. 6 that the curves in each case cross at $\varepsilon_1 + \varepsilon_2 = 1$, which verifies Eq. (20), i.e., $C_{\varepsilon_1} - C_{\varepsilon_2} \propto \left[\left(1-\varepsilon_2\right)^2 - \varepsilon_1^2\right] = 0\Big|_{\varepsilon_1+\varepsilon_2=1}$. It' also obtained that C_{ε_1} is larger than (or smaller than) C_{ε_2} if $\varepsilon_1 + \varepsilon_2 > 1$ (or $\varepsilon_1 + \varepsilon_2 < 1$), which verifies Eq. (21).

Optics EXPRESS

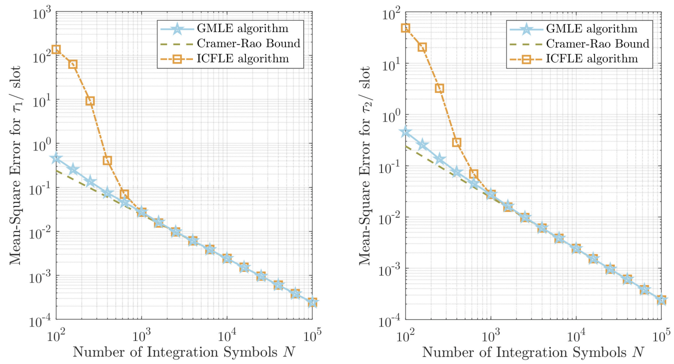

(a) Estimation for τ_1 (b) Estimation for τ_2

Fig. 4. MSE versus number of integration symbols N.

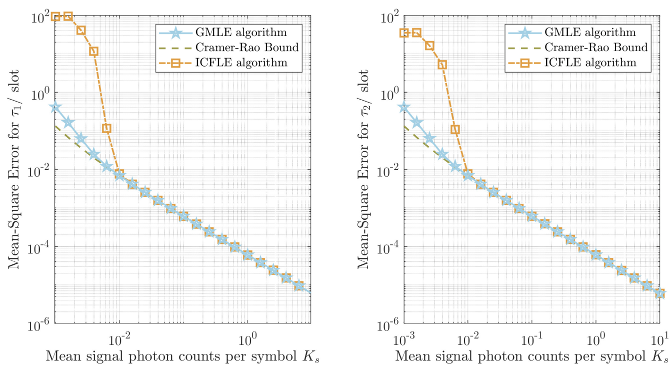

(a) Estimation for τ_1 (b) Estimation for τ_2

Fig. 5. MSE versus number of signal photon counts per symbol.

5.2. Experimental results

In this subsection, an equivalent experiment is built, which is shown in Fig. 7. As illustrated in Fig. 7, electrical signals from the AWG (Arbitrary Wave Generators, Tektronix 70002A) are first amplified and then modulated into optical signals. The product models of the amplifier, laser and modulator are IXblue DR-AN-10-MO, EM4 EM650, IXblue MX-LN-10-PD, respectively. Benefiting from analog characteristics of AWG's output, the AWG has the ability of simulating the Poisson distribution. The received optical signals are converted into current signals by the an APD, which are further converted into voltage signals with the help of the trans-impedance amplifier (TIA). The amplified electrical signal is finally collected by an oscilloscope (Tektronix DPO7354). To simulate a photon counting receiver, we first accumulate the sampled electrical signals in each time slot. The accumulated results are further normalized to the number of photons in each time slot. The normalized coefficient can be considered as a photon energy, which is chosen as $E_{\mathrm{equi}} = 0.00378V$ in this paper. Although this value may be much larger than the true energy of a photon after photoelectric conversion, this value serves as a benchmark in our equivalent experiment to normalize the rest of the values.

In order to build a 2×1 MISO system within a short distance, we utilize a beam-splitter with the splitting ratio to be 50:50. With the help of the beam-splitter, the optical signals from two transmitters are combined and further coupled into the receiver's fiber, which is depicted as the

Optics EXPRESS

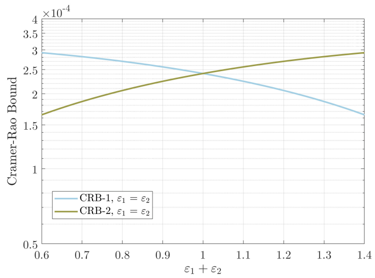

(a) $\varepsilon_1 = \varepsilon_2$ case

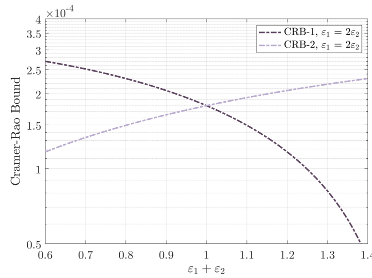

(b) $\varepsilon_1 = 2\varepsilon_2$ case.

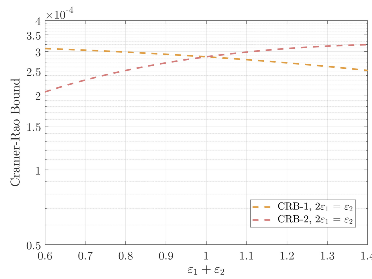

(c) $2\varepsilon_1 = \varepsilon_2$ case.

Fig. 6. The relationship of CRB-1 and CRB-2.

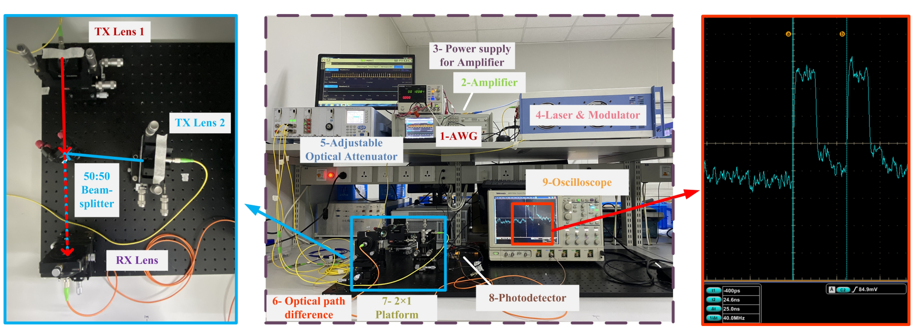

Fig. 7. 2×1 MISO platform(left), experimental scene (middle), verification of optical path difference(right).

blue line and the red line in the left part of Fig. 7. The adjustable optical attenuator (YOKOGAWA AQ2200) guarantees that the signals coupled into the fiber from two optical paths have the same power. The path difference $|\tau_1 - \tau_2|$ is created by an extra 5m long fiber. It's also mentioned that the timing offsets τ_1 and τ_2 can be adjusted by setting the start point of the acquisition process in the oscilloscope. In other words, the equivalent experiment is valid to simulate the practical scene with long distance. Since the refractive index of the fiber core is approximately 1.5, the path difference $|\tau_1 - \tau_2|$ brought by a 5m fiber is approximately 25ns, which can be verified in the right part of Fig. 7.

The MSE results of $\hat{\tau}_1$, $\hat{\tau}_2$, $|\hat{\tau}_2 - \hat{\tau}_1|$ are given in Figs. 8(a), 8(b) and 8(c), respectively. As can be seen from Fig. 8, the MSEs decrease with increasing integration symbols' number N. Besides, it's also observed that the GMLE outperforms ICFLE, where their gap gradually narrows with the increasing of N. These two phenomena are consistent with the previous simulation results in Sec.5.1.

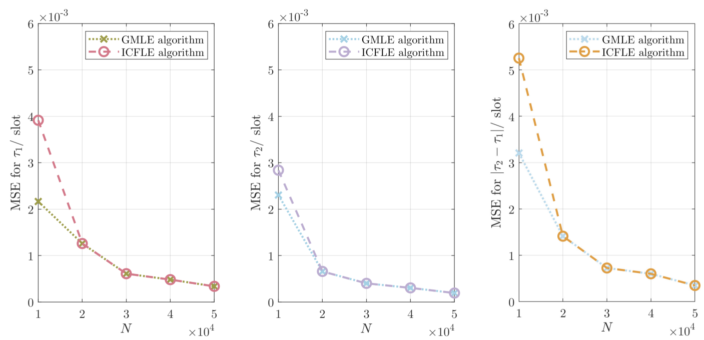

(a) (b) (c)

Fig. 8. MSE of estimated values in experiments.

In order to describe the estimation results more intuitively, we show 200 samples estimated by GMLE algorithm in Figs. 9(a) and 9(b), where N is set to be 10000 and 50000, respectively. The estimated samples consist of $\hat{\tau}_1$, $\hat{\tau}_2$ and $|\hat{\tau}_2 - \hat{\tau}_1|$. The similar conclusion can be drawn that the MSE of estimated values with larger $N(N = 50000)$ is smaller than the MSE of estimated values with fewer N ($N = 10000$). In addition, the mean values of $\hat{\tau}_1$, $\hat{\tau}_2$ are equal to 0.726 and 3.2425, respectively. What's more, the mean value of $|\hat{\tau}_2 - \hat{\tau}_1|$ is equal to 2.5165 slots. Due to the slot rate is set to be 100Msps, the precise value of offsets difference is 25.165ns, which verifies the rough value of 25ns in the right part of Fig. 7. So far, through the experimental results, we can conclude that our proposed GMLE and ICFLE algorithms are feasible and effective.

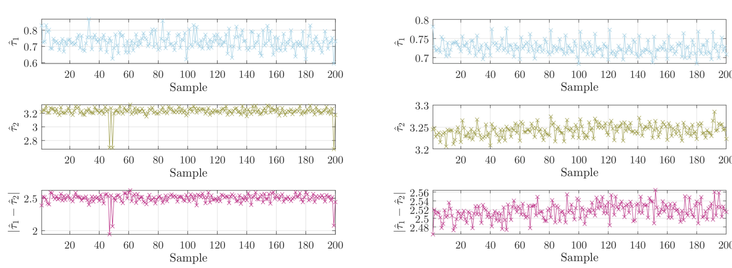

(a) $N = 10000$ (b) $N = 50000$

Fig. 9. Samples of estimated values by GMLE.

6. Conclusion

This paper is devoted to estimating the time offsets in 2×1 optical MISO PPM systems with photon-counting receivers. We first prove that the likelihood function is not differentiable at integer points, but is differentiable at every integer interval. Two estimation algorithms are further proposed, which are the optimal GMLE and the suboptimal ICFLE, respectively. According to the numerical results, both the two proposed algorithms has the ability of approaching the deduced CRBs under the condition of large SNR. Meanwhile, the GMLE algorithm outperforms ICFLE in low SNR situations, which results from the fact that estimated values' integer parts by ICFLE have a large probability to deviate from their true integer values in low SNR cases. It's also proved that the CRB C_{ε_1} is larger than (or smaller than) C_{ε_2} if $\varepsilon_1 + \varepsilon_2 > 1$ (or $\varepsilon_1 + \varepsilon_2 < 1$). An equivalent experiment is also built to verify the feasibility and effectiveness of the proposed algorithms. Besides, the complexity analyses imply that the proposed algorithms are potential to be utilized in practical systems.

Funding. National Natural Science Foundation of China (62101527); Changchun Institute of Optics, Fine Mechanics and Physics, Chinese Academy of Sciences (Funding Program of Innovation Labs).

Disclosures. The authors declare no conflicts of interest.

Data availability. Data underlying the results presented in this paper are not publicly available at this time but may be obtained from the authors upon reasonable request.

References

1. H. Kaushal and G. Kaddoum, "Optical Communication in Space: Challenges and Mitigation Techniques," IEEE Commun. Surv. Tutor. **19**(1), 57–96 (2017).
2. G. Xu and Z. Song, "Amplitude fluctuations for optical waves propagation through non-Kolmogorov coronal solar wind turbulence channels," Opt. Express **26**(7), 8566–8580 (2018).
3. M. S. Bashir and M. S. Alouini, "Signal Acquisition With Photon-Counting Detector Arrays in Free-Space Optical Communications," IEEE Trans. Wireless Commun. **19**(4), 2181–2195 (2020).
4. D. M. Boroson and B. S. Robinson, "The Lunar Laser Communication Demonstration: NASA's First Step Toward Very High Data Rate Support of Science and Exploration Missions," Space Sci. Rev. **185**(1-4), 115–128 (2014).
5. E. Sarbazi, M. Safari, and H. Haas, "Statistical Modeling of Single-Photon Avalanche Diode Receivers for Optical Wireless Communications," IEEE Trans. Commun. **66**(9), 4043–4058 (2018).
6. W. Zwoliński, M. Jarzyna, and K. Banaszek, "Range dependence of an optical pulse position modulation link in the presence of background noise," Opt. Express **26**(20), 25827–25838 (2018).
7. Y. Ata, Y. Baykal, and M. C. Gökce, "*M*-ary pulse position modulation performance in non-Kolmogorov turbulent atmosphere," Appl. Opt. **57**(24), 7006–7011 (2018).
8. S. Yu, C. Geng, J. Zhong, and D. Kang, "Performance analysis of optical spatial modulation over a correlated gamma-gamma turbulence channel," Appl. Opt. **61**(8), 2025–2035 (2022).
9. A. E. Abouelez, "Performance analysis of an *L*-ary PPM MISO ground-to-satellite free-space laser link with an APD-based receiver over a Málaga turbulence channel in the presence of beam wander," J. Opt. Commun. Netw. **14**(3), 100–110 (2022).
10. J. Xiang, Y. Jia, C. Deng, S. Huang, C. Li, X. Chen, P. Zhang, and Y. Wu, "Channel likelihood correction for photon-counting array receivers in the presence of dead time and jitters," Opt. Express **26**(3), 2848–2856 (2018).
11. G. Xu, "Error performance of deep space optical communication with M-ary pulse position modulation over coronal turbulence channels," Opt. Express **27**(9), 13344–13356 (2019).
12. K. Yan, S. Cheng, H. -C. Wu, H. Xiao, and X. Zhang, "Analysis and Rectification of the Asynchronous Sampling Effect in the Pulse-Position Modulation Systems," IEEE Sensors J. **20**(8), 4189–4199 (2020).
13. M. S. Bashir and S. S. Muhammad, "Time Synchronization in Photon-Limited Deep Space Optical Communications," IEEE Trans. Aerosp. Electron. Syst. **56**(1), 30–40 (2020).
14. R. Rogalin and M. Srinivasan, "Maximum Likelihood Synchronization for Pulse Position Modulation with Inter-Symbol Guard Times," *IEEE Global Communications Conference (GLOBECOM)*, 1–6 (2016).
15. X. Wang, L. Guo, L. Zhang, and Y. Liu, "Link design of Moon-to-Earth optical communication based on telescope array receivers," Opt. Commun. **310**, 12–18 (2014).
16. T. Özbilgin and M. Koca, "Polarization Diversity in MIMO Communication Over Atmospheric Turbulence Channels," J. Lightwave Technol. **34**(17), 3981–3992 (2016).
17. M. D. A. Mohamed and S. Hranilovic, "Diversity Reception for Deep-Space Optical Communication Using Linear Projections," IEEE J. Sel. Top. Quantum Electron. **16**(5), 1071–1083 (2010).
18. Y. Zhang, H. Yu, J. Zhang, Y. Zhu, J. Wang, and X. Ji, "On the Optimality of Spatial Repetition Coding for MIMO Optical Wireless Communications," IEEE Commun. Lett. **20**(5), 846–849 (2016).

Optics EXPRESS

19. E. E. Elsayed and B. B. Yousif, "Performance enhancement of the average spectral efficiency using an aperture averaging and spatial-coherence diversity based on the modified-PPM modulation for MISO FSO links," Opt. Commun. **463**, 125463 (2020).
20. X. Zhou, D. Zhang, R. Zhang, and L. Hanzo, "A photon-counting spatial-diversity-and-multiplexing MIMO scheme for Poisson atmospheric channels relying on Q-ary PPM," Opt. Express **20**(24), 26379–26393 (2012).
21. V. Dixit and A. Kumar, "Error analysis of L-PPM modulated MIMO based multi-user NOMA-VLC system with perfect and imperfect SIC," Appl. Opt. **61**(4), 858–867 (2022).
22. S. Boyd and L. Vandenberghe, *Convex Optimization*. (Cambridge University Press, NewYork, NY, USA, 2004).
23. H. L. V. Trees, K. L. Bell, and Z. Tian, *Detection Estimation and Modulation Theory, Part I: Detection, Estimation, and Filtering Theory*, 2nd Ed., (John Wiley & Sons, New Jersey, NJ., USA, 2013).